Materials Research Bulletin 153 (2022) 111912

Contents lists available at ScienceDirect

Materials Research Bulletin

journal homepage: www.elsevier.com/locate/matresbu

Research Papers

Experimental evaluation of the activity and selectivity of pure $MnWO_4$ and doped with rare earth ions in the CO_2 photoreduction process

Júlia C. Peixoto [a], André E. Nogueira [a], Anderson Dias [b], Juliana A. Torres [c], Jean C. da Cruz [c], Caue Ribeiro [c], Kisla P.F. Siqueira [a,*]

[a] Laboratory of Ceramic Materials and Raman Spectroscopy, Department of Chemistry, Federal University of Ouro Preto (UFOP), Campus Morro do Cruzeiro, ICEB II, Ouro Preto, MG 35400-000, Brazil

[b] Department of Chemistry, ICEx, Federal University of Minas Gerais (UFMG), Belo Horizonte, MG 31270-901, Brazil

[c] Embrapa Instrumentation, Rua XV de Novembro, 1452, São Carlos, SP 13560-970, Brazil

ARTICLE INFO

Keywords:
Manganese tungstate
Doping
Rare earth
CO2 photoreduction
Selectivity

ABSTRACT

The reduction of CO_2 to produce useful carbon compounds offers a way to manage the emissions from various industrial sectors. However, selecting efficient systems remain a crucial issue, especially considering the low selectivity of the photocatalysts traditionally used in CO_2 photoreduction processes. Here we demonstrate that the modification of $MnWO_4$ with rare earth ions (Europium and Terbium) synthesized by the coprecipitation method can tune the activity and selectivity of the products formed in the process of CO_2 photoreduction under UV irradiation. The CO_2 photoreduction assays indicated that the photocatalysts presented good activity, resulting in acetate, acetone, acetic acid, ethanol, methane, and methanol products. Doping provided selectivity near 100% for CO_2 conversion to methanol and increased the capacity of C2 (e.g., ethanol) production, opening the way for a better understanding of the activity and selectivity of tungstates in the CO_2 photoreduction process.

1. Introduction

Carbon dioxide is one of the main greenhouse gases, and its largest source of emission is the burning of non-renewable fossils [1, 2, 3]. Consequently, there have been many studies concerning the conversion of CO_2 to reduce the concentration of this gas in the atmosphere [4, 5, 6]. CO_2 reduction reactions can be used to produce compounds such as formic acid (HCOOH), methane (CH_4), and methanol (CH_3OH), considered renewable sources of energy [2]. The main techniques currently used for CO_2 conversion are thermocatalysis [7], enzymatic processes [8], photocatalysis, photoelectrocatalysis, and electrocatalysis. Photocatalytic CO_2 reduction, especially, has attracted attention due to the possibility of sustainable use of solar energy and the fact that heterogeneous catalysts can be recycled [1]. Thus, many advances have been made recently in the area of artificial photosynthesis of CO_2 in order to explore more efficient photocatalysts for CO_2 reduction [9, 10, 11, 12, 13, 14, 15, 16]. The literature reports applications of different classes of materials used as photocatalysts in the conversion of CO_2 [17, 18, 19, 20, 21], including tungstates such as $Ag/AgWO_4$ [22], $CuWO_4$ [23], $Ni_{0.85}Co_{0.15}WO_4$ [1], γ-$C_3N_4/FeWO_4$ [24], and Bi_2WO_6 [25–26].

Manganese tungstate, known as Hubnerite [27], has excellent optical, electrical, and magnetic properties [28,29]. $MnWO_4$ is suitable for photocatalytic applications since it presents an energy band gap of around 2.7 eV, so it can generate a photoresponse when exposed to visible light [28,30]. Furthermore, the valence band (VB) and the conduction band (CB) have suitable potentials (VB = +3.10 V, CB = +0.47 V vs NHE) [31]. For the use of a semiconductor as a photocatalyst, the conduction band must have a sufficiently negative reduction potential to drive the photoreduction reaction. Likewise, the valence band must have a sufficiently positive reduction potential to carry out the photo-oxidation reaction. For example, in the photoreduction process, when the semiconductor VB position is more positive than the H_2O/H^+ potential (+2.32 V vs. NHE, pH 7.0) and the CB position is more negative than the H^+/H_2 potential (-0.41 V vs. NHE, pH 7.0) or CO_2/CH_4 (-0.24 V vs. NHE, pH 7.0), CO_2 reduction may occur [32]. Thus, electrons in the conduction band of $MnWO_4$ (+0.47 V NHE) cannot reduce O_2, H^+, or CO_2 through a single electronic process, which limits the photocatalytic performance of $MnWO_4$ [33], although experimental studies have demonstrated its activity in photoreduction processes [34]. Joaquín-Morales et al. [28] carried out a study on the effect of synthesis

* Corresponding author.
E-mail address: kisla@ufop.edu.br (K.P.F. Siqueira).

https://doi.org/10.1016/j.materresbull.2022.111912
Received 6 March 2022; Received in revised form 23 May 2022; Accepted 24 May 2022
Available online 26 May 2022

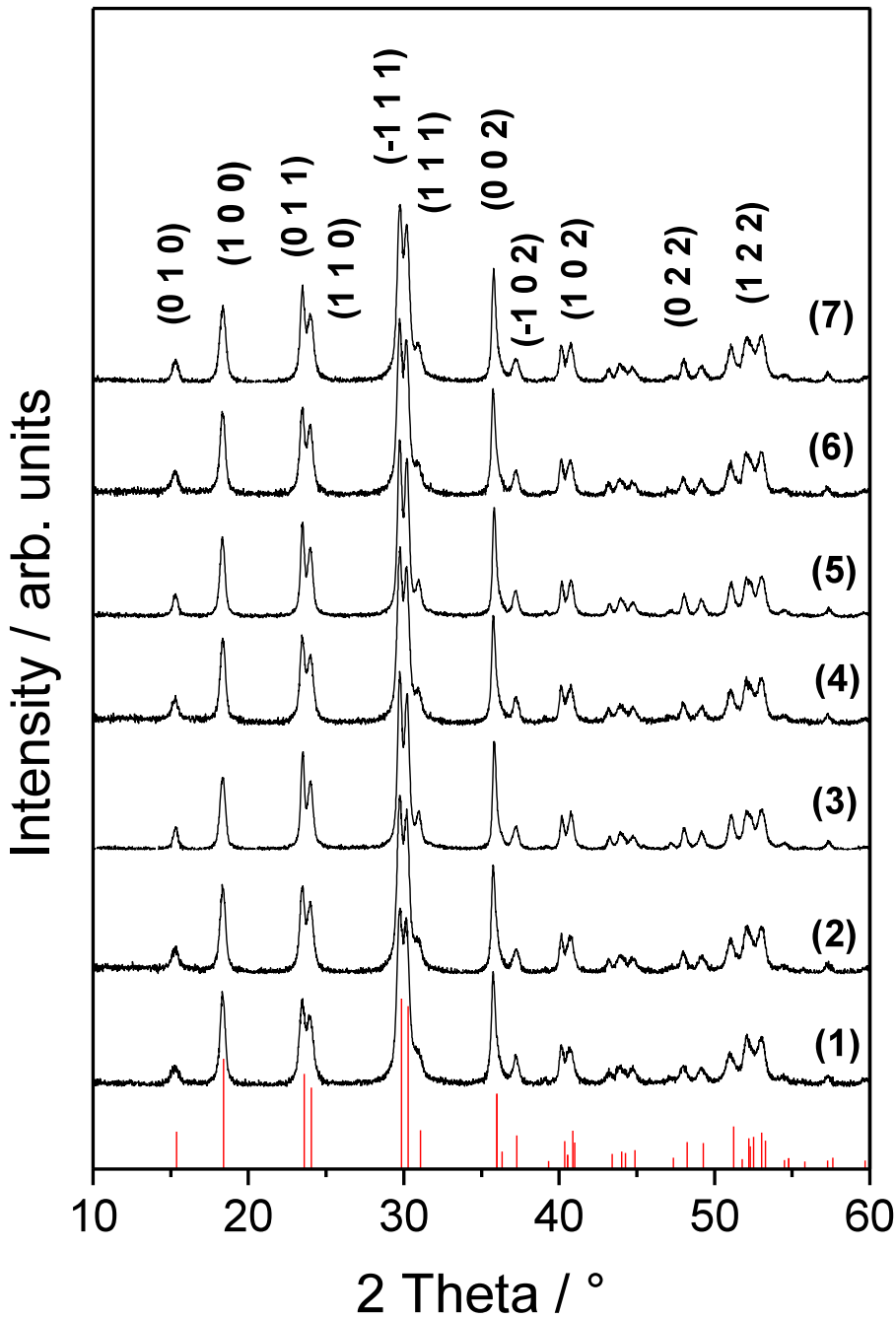

Fig. 1. Diffractograms of the synthesized photocatalysts: (1) $MnWO_4$, (2) Eu0.5, (3) Eu1.0, (4) Tb0.5, (5) Tb1.0, (6) Eu/Tb0.5, and (7) Eu/Tb1.0. The ICSD #00-080-0152 standard, corresponding to $MnWO_4$, is shown in red.

conditions (coprecipitation) on the photocatalytic properties of $MnWO_4$ for the production of H_2 by waterspllitting under visible irradiation. The study revealed that $MnWO_4$ (1%-UT) produced the highest amount of H_2 among all samples with a value of 72 $mmolH_2g^{-1}$, which was much higher compared to WO_3, used as a reference photocatalyst. They attributed this behavior to the greater surface area available about other synthesized materials, concluding that $MnWO_4$ is a promising material for applications in photocatalysis aiming at the production of H_2.

One of the major challenges to CO_2 photoreduction is the product selectivity, i.e., the ability of a given catalyst to produce a single product, avoiding further separation and maximizing the reaction efficiency. The complex structure of tungstates makes them adequate for doping, and that strategy could interfere with the CO_2 bonding at the catalyst's surface. Significantly, the large electronic shell of rare earth ions could be interesting to promote specific interactions that have not been investigated yet. Thus, here we synthesized Eu^{3+} and/or Tb^{3+} -doped $MnWO_4$, using the coprecipitation method, evaluating their activity and selectivity in the CO_2 photoreduction process. Our results revealed that doping increases the selectivity to methanol up to 100%, and in adequate conditions, leads to remarkable ethanol production, showing that the doping can do a "tuning" effect worth investigation.

2. Materials and methods

2.1. Synthesis procedures

The photocatalysts were synthesized by coprecipitation, using the precursors sodium tungstate dihydrate ($Na_2WO_4.2H_2O$, 99-101%,

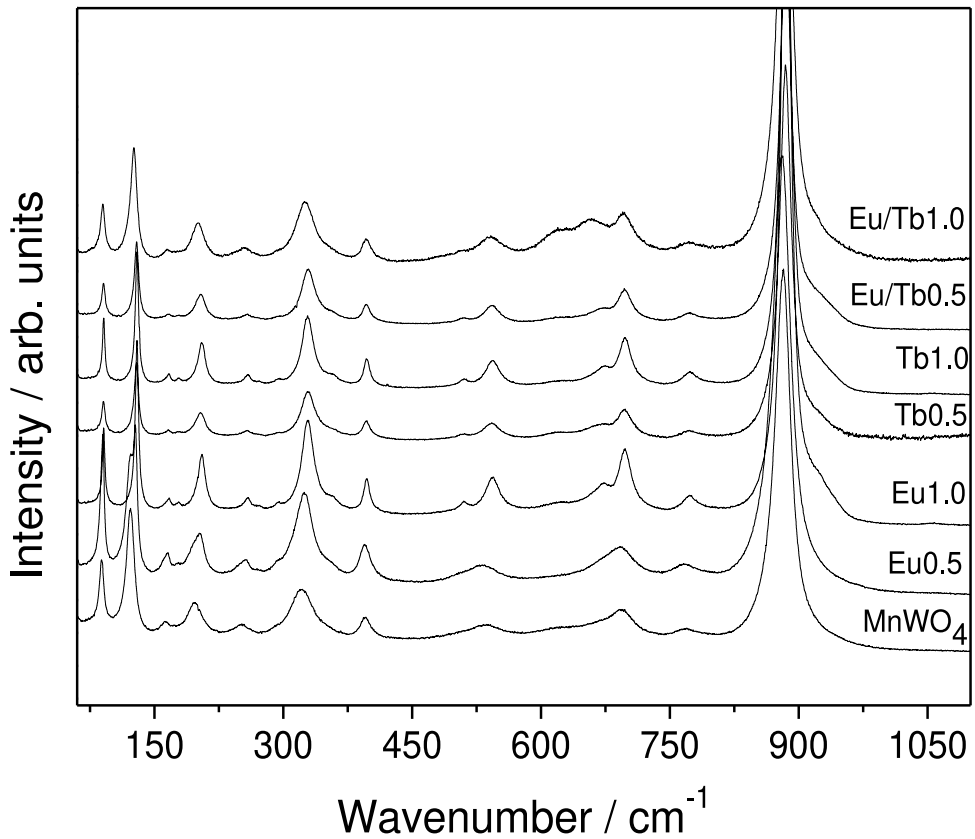

Fig. 2. Raman spectra of the pure $MnWO_4$ and the photocatalysts modified by doping with europium and terbium at 0.5 and 1.0 mol%.

Synth) and manganese (II) chloride tetrahydrate ($MnCl_2.4H_2O$, 98-101%, Synth). The catalysts were modified with the rare earth ions europium (Eu^{3+}) and/or terbium (Tb^{3+}), in amounts of 0.5 and 1.0 mol %, employing terbium chloride hexahydrate ($TbCl_3.6H_2O$, 99.9%, Sigma-Aldrich) and europium chloride hexahydrate ($EuCl_3.6H_2O$, 99.9%, Sigma-Aldrich) as the metal precursors.

Stoichiometric amounts of the precursors were solubilized in distilled water, followed by pouring the rare earth ion solution into the $MnCl_2$ solution, and then pouring into the Na_2WO_4 solution. The resulting solution was kept under agitation for several minutes, for complete homogenization of the solution and precipitation of the product. The material was then washed several times with distilled water, in order to remove the salts (reaction byproducts) by decantation. Finally, the material was dried in an oven at 100°C and macerated for complete homogenization. The synthesized photocatalysts were named according to the rare earth ions present and the corresponding doping content (in mol%), as follows: $MnWO_4$ for the pure photocatalyst, Eu0.5 ($Eu^{3+}_{0.5\%}$:$MnWO_4$), and Eu1.0 ($Eu^{3+}_{1.0\%}$:$MnWO_4$) for the materials modified with europium ions, Tb0.5 ($Tb^{3+}_{0.5\%}$:$MnWO_4$) and Tb1.0 ($Tb^{3+}_{1.0\%}$:$MnWO_4$) for the materials modified with terbium ions, and Eu/Tb0.5 ($Eu^{3+}_{0.25\%}Tb^{3+}_{0.25\%}$:$MnWO_4$) and Eu/Tb1.0 ($Eu^{3+}_{0.5\%}Tb^{3+}_{0.5\%}$:$MnWO_4$) for the photocatalysts modified with both rare earth ions.

2.2. Characterization

The crystalline structures of the photocatalysts were investigated by X-ray diffraction (XRD), using a PANalytical X'Pert3Powder instrument operated at 45 kV and 40 mA, with Cu *K*α radiation (λ = 1.54059 Å) and scanning angle (2Θ) from 10° to 60°. The diffractograms were compared with reference standards from the Inorganic Crystal Structure Database (ICSD), using QualX software [35].

The vibrational modes of the photocatalysts were investigated by Raman spectroscopy, using a Horiba/Jobin-Yvon LABRAM-HR spectrometer coupled to an Olympus confocal microscope. The system included a He-Ne excitation laser (λ = 632.8 nm) with a nominal power of 18 mW, edge filters to remove Rayleigh scattering, and a charge-coupled device (CCD) with Peltier cooling. Spectra were acquired in the range from 60 to 1100 cm^{-1}, using a 100 × objective lens and a diffraction grating with 1800 lines/mm.

Morphological analysis of the photocatalysts was performed by scanning electron microscopy (SEM), using a Quanta 200 FEG microscope (FEI) with an applied voltage of 15 kV. The micrographs were processed using GNU Image Manipulation Program v. 2.6.11 software (Free Software Foundation, Boston, MA, USA). Determination of the gap energy (E_{gap}) of the photocatalysts and investigation of their absorption bands employed diffuse reflectance spectroscopy (DRS), using a Shimadzu UV-2600 instrument operated in the ultraviolet-visible region between 200 and 800 nm, in average scan mode.

2.3. CO_2 photoreduction

The CO_2 photoreduction assays were performed using 100 mg of sample in 100 mL of distilled water, for a period of 6 h, under UV-C irradiation from six Osram lamps (15 W, 254 nm). Saturation of the reaction system was achieved by providing a flow of high purity CO_2 for 10 min. The samples were dispersed in 150 mL quartz tubes fitted with septa to allow entry of CO_2 and collection of gaseous products. The reaction was kept under constant stirring, at 15°C, using a thermostatic bath. After the reaction, the liquid products were identified and quantified by ^1H nuclear magnetic resonance (NMR) (600 MHz, Ascend™ 600, Bruker), at 25°C. For this, a 540 μL volume of the sample was mixed with 60 μL of D_2O solution containing 5 mmol L^{-1} dimethyl sulfoxide (DMSO) as an internal standard and 0.21 mmol L^{-1} TSPd4 as a reference. The WET procedure was used to suppress the water peak and the NMR data were processed using MestReNova software [36]. The gas-phase products generated were analyzed by gas chromatography

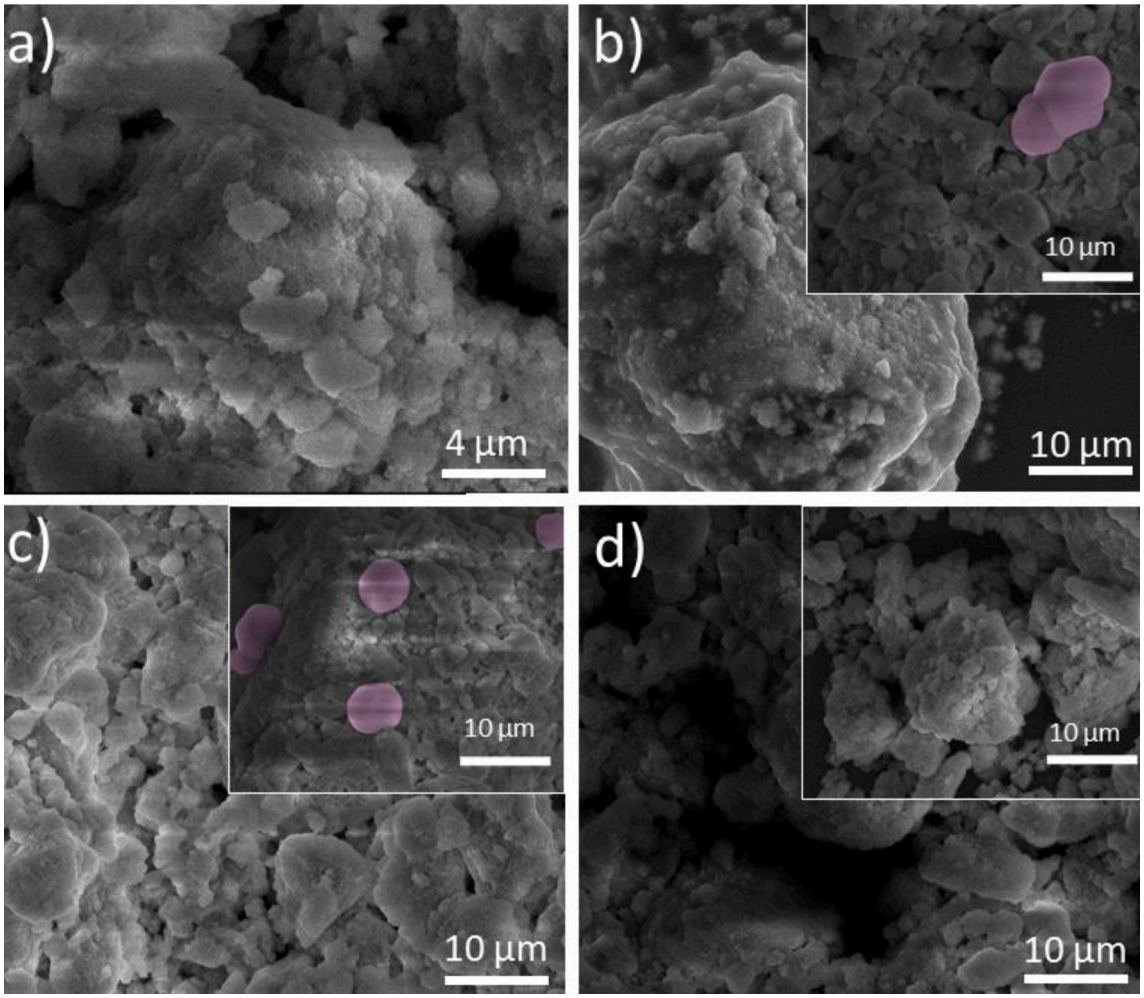

Fig. 3. SEM micrographs of the synthesized photocatalysts: a) $MnWO_4$, b) Eu0.5 (with Eu1.0 in the inset), c) Tb0.5 (with Tb1.0 in the inset), and d) Eu/Tb0.5 (with Eu/Tb1.0 in the inset).

(Trace 1310, Thermo), using molecular sieve 13X and Porapack N columns. The carrier gas was argon, and flame ionization (FID) and thermal conductivity (TCD) detectors were kept at 150°C and 200°C, respectively. Three control experiments were performed: i) without catalyst, under irradiation; ii) with catalyst, in the dark; and iii) using a flow of N_2, rather than CO_2.

3. Results and discussion

3.1. Characterization of the manganese tungstates

Fig. 1 shows all the diffractograms for the pure and modified manganese tungstate, which were indexed using the ICSD #00-080-0152 standard, corresponding to the $MnWO_4$ phase. All the photocatalysts crystallized in a monoclinic arrangement, of the wolframite type, belonging to the *P2/c* (#13) space group with two units per unit cell. All the diffractograms obtained were similar, indicating that there was no presence of secondary phases and/or impurities, confirming the success of the synthesis. The similarity among the diffractograms could be explained by the low doping contents used to modify the photocatalysts (0.5 or 1.0 mol%), which did not significantly affect the organization of the atoms or the positions of the crystallographic planes.

The crystallite sizes of the materials were estimated using the Scherrer equation:

$$D = \frac{K.\lambda}{\beta \mathrm{Cos}\theta} \tag{1}$$

where K is the Scherrer constant (0.9), λ is the wavelength of the Cu*K*α radiation (0.154 nm), β is the peak width (in radians) at half height, and θ is the Bragg angle (in radians) [37]. Calculation of the crystallite sizes employed the (100), (-111), and (002) planes, obtaining an average value of approximately 19 nm. All the values for the photocatalysts are provided in Table S1 (Supplementary Material). The sizes for the different samples were very similar and agreed with the literature values for $MnWO_4$ synthesized by coprecipitation [37,38].

As noted above, all the synthesized photocatalysts crystallized in a monoclinic structure, belonging to the *P2/c* (#13) space group and the C_{2h} point group. In this configuration, the Mn and W ions with C_2 symmetry occupy the Wyckoff positions 2*f* and 2*e*, respectively, while the oxygen ions with C_1 symmetry occupy the 4*g* site. Hence, by using the group theory [39], it was possible to obtain the following distribution of modes: $\Gamma = 8A_g + 10B_g + 8A_u + 10B_u$, with 18 Raman-active modes ($8A_g + 10B_g$), 15 infrared-active modes ($7A_u + 8B_u$), and 3 acoustic modes ($A_u + 2B_u$) [40,41]. Fig. 2 shows the Raman spectra at ambient temperature for the photocatalysts, revealing the presence of all the 18 predicted modes. A band centered at around 885 cm^{-1} (A_g) corresponded to the symmetric stretching vibration of the short terminal W−O bond, while a band at 774 cm^{-1} (B_g) represented the asymmetric stretching vibration of the short W−O bond [42]. The two bands at 674 cm^{-1} (B_g) and 698 cm^{-1} (A_g) could be attributed to asymmetric

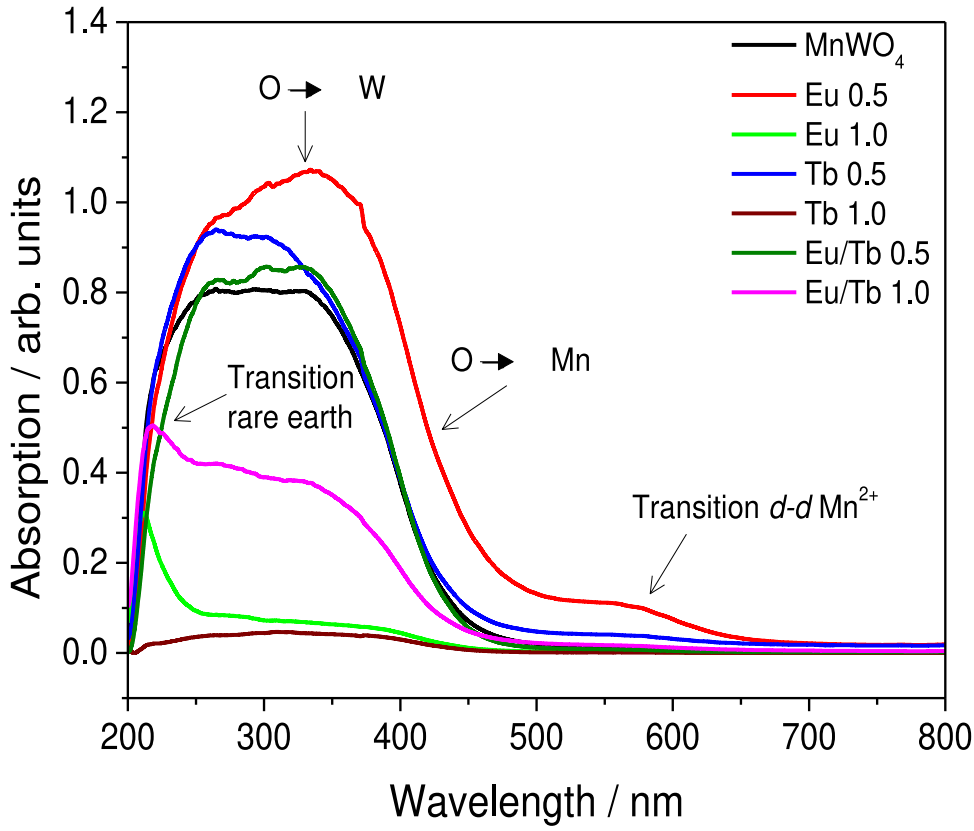

Fig. 4. Spectra of absorbance, as a function of wavelength, for the pure $MnWO_4$ and the modified photocatalysts.

stretching vibration modes of the longer W−O bonds in the $(W_2O_4)_n$ groups [42,43]. A band at 512 cm^{-1} (B_g) corresponds to the symmetric stretching vibration of the longer W−O bonds, while the band at 397 cm^{-1} (A_g) corresponds to the bending vibration of the short W−O bonds. The vibrational modes of the Mn−O bonds were represented by three bands at 294, 327, and 356 cm^{-1}. The remaining six bands at 129, 166, 177, 206, 258, and 272 cm^{-1} are related to the between-chain deformation modes and lattice modes [42].

Table S2 provides the wavenumbers of the vibrational modes for all the synthesized materials, together with their respective assignments, based on data reported by Ruiz-Fuertes et al. [44] and Siqueira et al. [45] for pure $MnWO_4$. In general, the vibrational modes tend to shift to higher wavenumbers after the insertion of the rare earth ions into the structures [46,47]. These shifts are expected, since the presence of the dopants sharing the manganese ion sites caused short-range perturbation of the crystalline lattice, due to the difference in the ionic radii. In this case, the rare earth ions Eu^{3+} (0.947 Å) [41] and Tb^{3+} (0.923 Å) [48] presented greater ionic radii, compared to the Mn^{2+} ion (0.83 Å) [49].

Fig. 3 shows the SEM micrographs obtained for all the synthesized photocatalysts. It can be seen that the pure and modified materials had similar morphologies, with irregular surfaces and variable particle sizes, characteristic of the synthesis process employed. The coprecipitation process involves steps of nucleation, agglomeration, and particle growth, which consequently influence the final particle morphology and size [50]. In the case of the photocatalysts doped at 1.0 mol% (Eu1.0 and Tb1.0), there was the formation of some agglomerations with a spherical appearance on the surfaces of the materials, highlighted (in pink) in the insets of Fig. 3b and Fig. 3c. We suggest that the presence of these particles could have been related to the method used in the preparation of the samples and the random choice of the analysis region.

The influence of doping on the band gap energy of $MnWO_4$ was investigated using diffuse reflectance analysis (Fig. 4). It was possible to identify four regions of electronic transitions. A region of higher absorption at around 300 nm was related to the transition 2*p* (O) → 5*d* (W) [51], while absorption near 400 nm corresponds to the transition 2*p* (O) → 3*d* (Mn). A lower intensity region near 550 nm corresponds to the spin-forbidden transition of an electron from the e_g orbital to the T_{2g} orbital, commonly known as *d-d* electronic transitions of Mn^{2+} ($3d^5$) [42,52]. Transitions associated with the rare earth ions could be seen at around 230 nm, which were more pronounced in the spectra of samples with higher doping contents (1.0 mol%). As proposed by Hammer et al. [53], the O → Eu transition could occur for the samples doped with europium ions, while those doped with terbium could present the 4*f* → 5*d* transition of the terbium ion itself.

The band gap energy for each synthesized photocatalyst was calculated based on the method proposed by Wood and Tauc [54] and the Kubelka-Munk function [38,55], as described in the Supplementary Material. Fig. 5 shows the corresponding E_{gap} values for the materials. The band gap energy values obtained were close to those reported in the literature, which ranged from 2.4 to 3.0 eV [38,56]. The modified photocatalysts generally presented values slightly lower than for the pure $MnWO_4$, except for Tb0.5 and Eu/Tb0.5, for which the E_{gap} values were the same as for the pure photocatalyst. As shown in Fig. 5, for the materials doped with europium ions, the E_{gap} value remained almost unchanged with an increase in the doping content. For the materials doped with terbium and europium/terbium ions, the E_{gap} values showed a slightly decreasing trend as the doping content increased. It is suggested that the slight change in band gap values may be correlated with the doping process of the material.

3.2. Photocatalytic performance evaluation

The reduction of CO_2 under UV irradiation was used to evaluate the performances of the pure $MnWO_4$ and the materials modified with Eu^{3+} and Tb^{3+} ions (Fig. 6). Three control experiments were previously

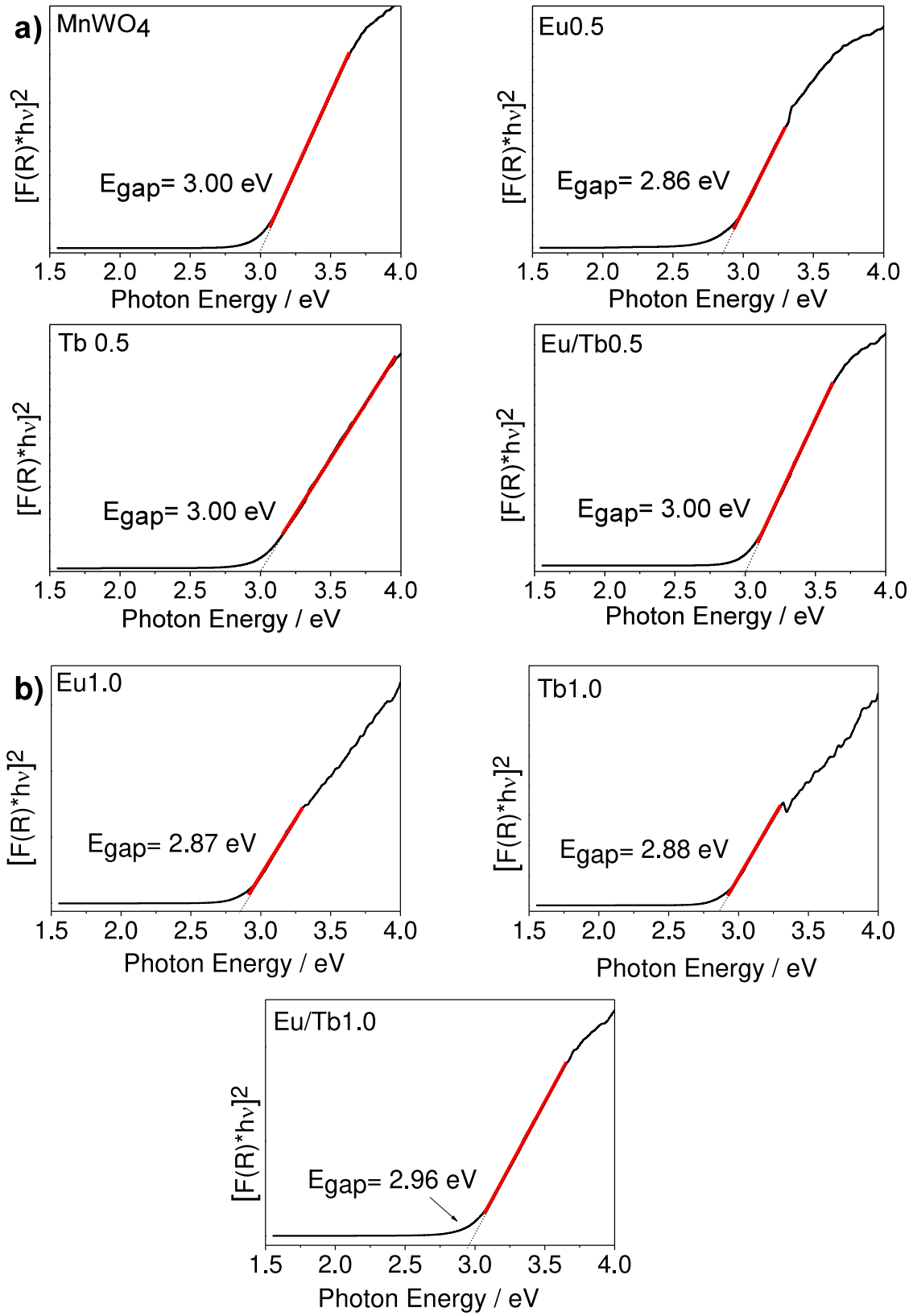

Fig. 5. (a) Band gap energies for $MnWO_4$ and the photocatalysts modified with 0.5 mol% of the rare earth ions. (b) Band gap energies for the photocatalysts modified with 1.0 mol% of the rare earth ions.

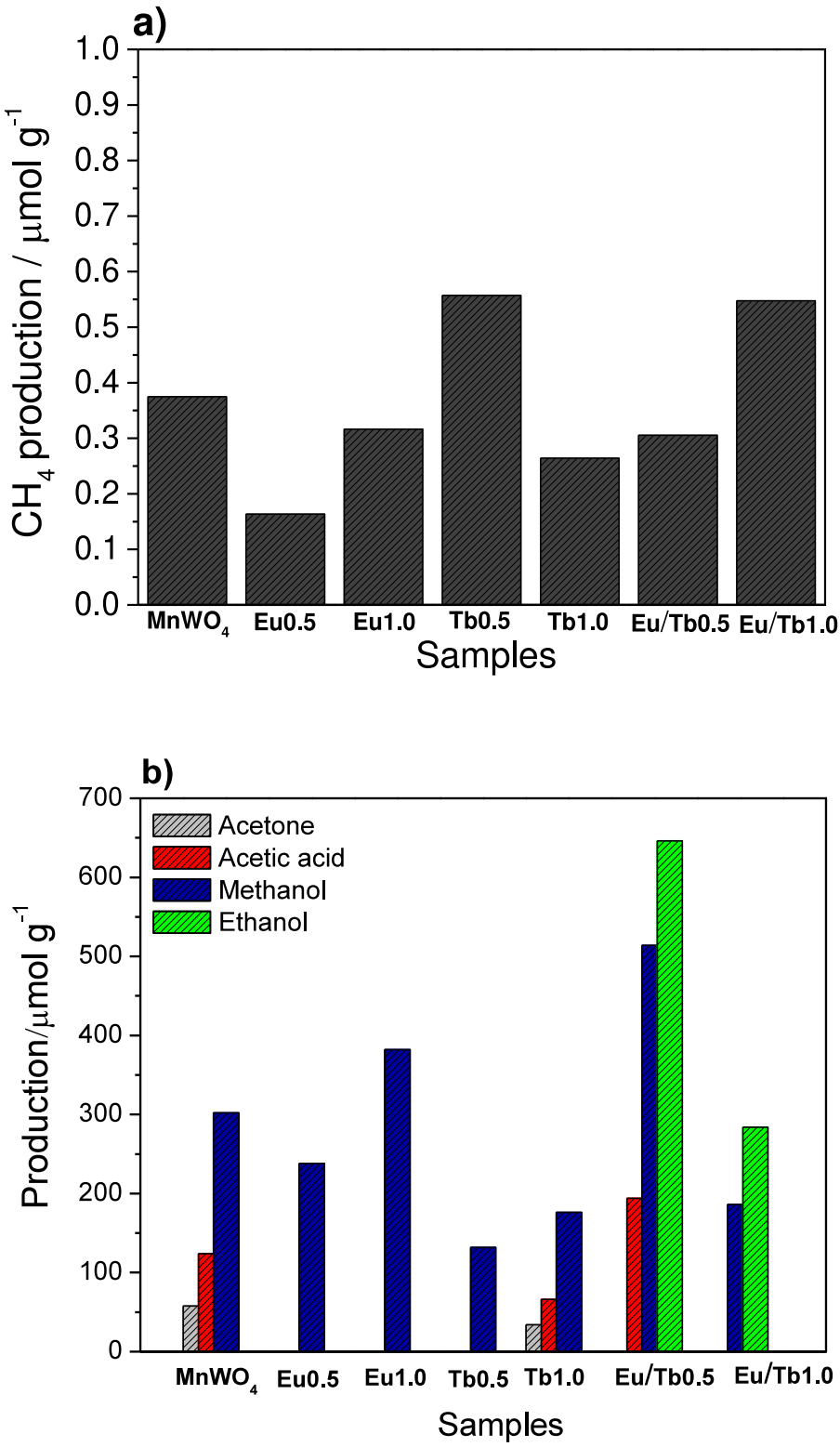

Fig. 6. Products were obtained in a) the gas phase and b) the liquid phase, from the photoreduction of CO_2 under UV irradiation, employing the materials synthesized in this work: $MnWO_4$, Eu0.5, Eu1.0, Tb0.5, Tb1.0, Eu/Tb0.5, and Eu/Tb1.0.

performed: i) without catalyst, under irradiation; ii) with catalyst, in the dark; and iii) using N_2 instead of CO_2, under the same reaction conditions as the CO_2 photoreduction. Only experiment i) showed the generation of a minimal amount of methane in the gaseous part of the reactor after 6 h of reaction, which was deducted from the activities of the materials, while there was no presence of liquid phase products. It is important to emphasize that all investigated materials showed good light exposure capacity and can be considered photostable.

Fig. 6a shows the photocatalytic performances of the synthesized materials in the reduction of CO_2 to CH_4. Despite the low concentrations produced, there was a preference for the formation of this gas-phase product, with no presence of other gaseous products such as CO and

Table 1
Selectivities towards the products generated in the CO_2 photoreduction.

Selectivity (%) Samples	Acetone	Acetic acid	Ethanol	Methane	Methanol
$MnWO_4$	11.8	18.9	0	0.114	69.2
Eu0.5	0	0	0	0.092	99.9
Eu1.0	0	0	0	0.110	99.9
Tb0.5	0	0	0	0.560	99.4
Tb1.0	12.1	17.6	0	0.141	70.2
Eu/Tb0.5	0	10.0	50.1	0.032	39.9
Eu/Tb1.0	0	0	60.3	0.155	39.5

H_2, which are commonly found in CO_2 photoreduction processes. As shown in Fig. 6b, there was a greater conversion of CO_2 to soluble products, rather than those in the gas phase, with the generation of compounds including acetone, acetic acid/acetate, ethanol, and methanol, as shown in the NMR spectra (Fig. S1). The results revealed that the incorporation of rare earth ions into the $MnWO_4$ structure altered both the selectivity and the efficiency of the material (see the calculation quantum yield in the Supplementary Material).

The selectivity of the synthesized materials in the conversion of CO_2 was calculated as described in the Supplementary Material, based on previous studies [57, 58, 59, 60, 61]. Table 1 shows the selectivities of the materials for different products (acetone, acetic acid, ethanol, methanol, and methane). The doped photocatalysts Eu0.5, Eu1.0, and Tb0.5 were highly selective (~99%) towards methanol production. On the other hand, the photocatalysts doped with both rare earth ions (Eu/Tb0.5 and Eu/Tb1.0) exhibited lower selectivity towards methanol, with the formation of other products such as ethanol and acetic acid.

Fig. 7 shows the rates of transfer of electrons involved in the photocatalytic reduction of CO_2 under UV irradiation, for 6 h. Although Tb0.5 presented high selectivity (~99.4%) for the conversion of CO_2 to methanol, this material exhibited the lowest electron transfer rate (132 e-/h). This rate followed the order Eu/Tb0.5 > Eu/Tb1.0 > $MnWO_4$ > Eu1.0 > Tb1.0 > Eu0.5 > Tb0.5. The Eu/Tb0.5 material exhibited the best activity, with an electron transfer rate of approximately 1290 e-/h, which was approximately 3 times higher than for the pure $MnWO_4$.

The doping of $MnWO_4$ with Eu^{3+} and Tb^{3+} ions led to a decrease in the electron transfer rate in the CO_2 photoreduction process, compared to the pure material, while these materials were more selective towards the production of methanol. This decrease could be attributed to the presence of defects in the structure of the materials that created recombination centers, resulting in rapid electron-hole pair recombination and, consequently, low photoactivity. However, the simultaneous incorporation of the two rare earth ions in the $MnWO_4$ structure may have suppressed these recombination centers, consequently increasing the electron transfer rate, as observed for the Eu/Tb0.5 material [62,63]. The presence of the combined dopants in the $MnWO_4$ structure resulted in the formation of higher hydrocarbons such as ethanol, which can be attributed to the generation of different adsorption sites on the surface of the material.

The CO_2 molecule has a linear structure (O=C=O), in which each of the oxygen atoms has a single pair of electrons that can be donated to Lewis acid sites present on the surface of the material. On the other hand, if the materials have Lewis acidic sites, the carbon atom of CO_2 can receive these electrons forming carbonate-like species [64]. In addition, if the material has basic and acidic sites, acting simultaneously as a donor and electron acceptor, mixed coordination with the CO_2 molecule can be formed, generating partially charged species on the surface of the material considered as key intermediates to produce a C2 product such as ethanol through the dimerization process of the adsorbed species [65]. Hence, it was clear that the type and amount of dopant were crucial in determining the activity and selectivity of the $MnWO_4$ since these factors affected the photogenerated charge recombination rate and the structure of the manganese tungstate band.

Conclusions

In this work, we synthesized several $MnWO_4$ materials doped and undoped with rare earth ions Eu^{3+} and/or Tb^{3+} by the coprecipitation method, to improve activity and selectivity in the CO_2 photoreduction process. All the materials were characterized using XRD, Raman, SEM, and DRS techniques, which confirmed the incorporation of the doping ions and no formation of heterostructures or secondary phases. The

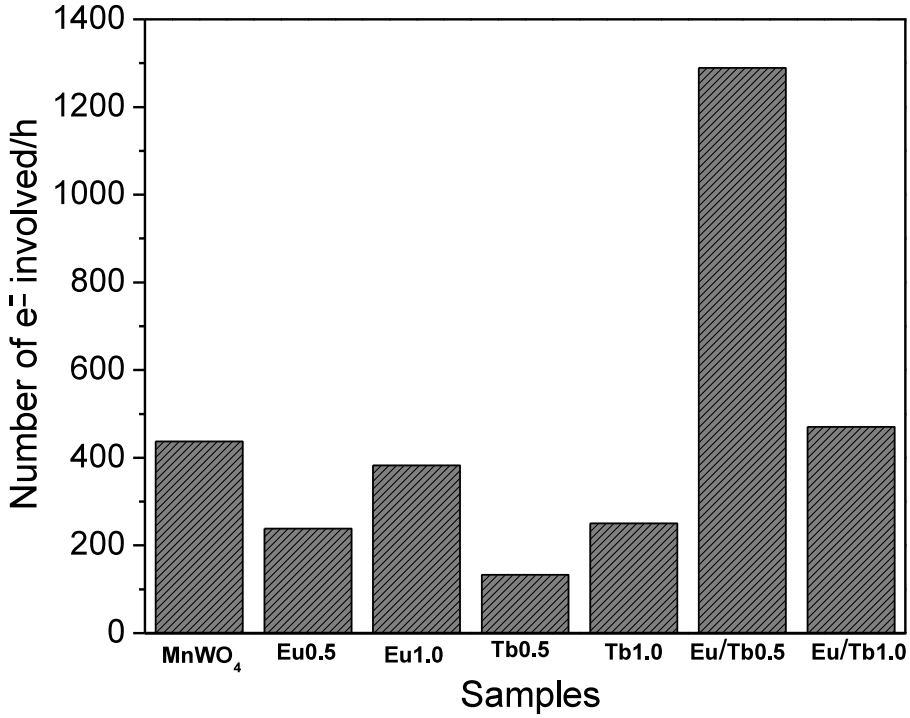

Fig. 7. Numbers of electrons involved in the process of photoreduction of CO_2 under UV irradiation.

results showed that the doping led to greater selectivity towards the formation of certain liquid products, while the materials doped with both rare earth ions (Eu/Tb0.5 and Eu/Tb1.0) were the only ones that showed selectivity towards the formation of ethanol. Furthermore, Eu/Tb0.5 presented the highest efficiency in the photoreduction of CO_2, which could be attributed to decreased recombination of photogenerated electron-hole pairs, due to the incorporation of the rare earth ion into the $MnWO_4$ structure. However, Eu/Tb0.5 presented low selectivity for products generated in the reaction medium, compared to the materials modified only with Eu (Eu0.5 and Eu1.0). Thus, these experimental results provide new insights into the behavior of tungstates used for CO_2 photoreduction.

CRediT authorship contribution statement

Júlia C. Peixoto: Methodology, Formal analysis, Investigation, Writing – original draft. **André E. Nogueira:** Methodology, Formal analysis, Writing – review & editing. **Anderson Dias:** Methodology, Writing – review & editing. **Juliana A. Torres:** Methodology, Writing – review & editing. **Jean C. da Cruz:** Methodology. **Caue Ribeiro:** Methodology, Writing – review & editing. **Kisla P.F. Siqueira:** Conceptualization, Writing – review & editing, Supervision, Funding acquisition.

Declaration of Competing Interest

The authors declare that they have no known competing financial interests or personal relationships that could have appeared to influence the work reported in this paper.

Acknowledgments

The authors are grateful for financial support provided by the Brazilian agencies Conselho Nacional de Desenvolvimento Científico (CNPq), Fundação de Amparo à Pesquisa do Estado de Minas Gerais (FAPEMIG), and Fundação de Amparo à Pesquisa do Estado de São Paulo (grants#381187/2021-7, 2018/01258-5, 2016/21515-7). The Center of Microscopy at the Universidade Federal de Minas Gerais (http://www.microscopia.ufmg.br) is also acknowledged for providing the equipment and technical support for experiments involving electron microscopy. This work was also supported by Universidade Federal de Ouro Preto (UFOP). Special thanks are due to Dr. Henrique S. Oliveira for DRS measurements.

Supplementary materials

Supplementary material associated with this article can be found, in the online version, at doi:10.1016/j.materresbull.2022.111912.

References

[1] C. Guo, B. Guo, X. Gao, J. Liang, Q. Meng, J. Liu, $Ni_{0.85}Co_{0.15}WO_4$ for photocatalytic reduction of CO_2 under mild conditions with high activity and selectivity, Catal. Lett. 150 (2020) 3071–3078.
[2] X.Y. Kong, W.L. Tan, B. Ng, S. Chai, A.R. Mohamed, Harnessing Vis – NIR broad spectrum for photocatalytic CO_2 reduction over carbon quantum dots-decorated ultrathin Bi_2WO_6 nanosheets, Nano Res. 10 (5) (2017) 1720–1731.
[3] J. Hou, S. Cao, Y. Wu, F. Liang, Y. Sun, Z. Lin, L. Sun, Simultaneously efficient light absorption and charge transport of phosphate and oxygen-vacancy confined in bismuth tungstate atomic layers triggering robust solar CO_2 reduction, Nano Energy 32 (2017) 359–366.
[4] L. Yuan, Y.-J. Xu, Photocatalytic conversion of CO_2 into value-added and renewable fuels, Appl. Surf. Sci. 342 (2015) 154–167.
[5] L. Yuan, S.-F. Hung, Z.-R. Tang, H.M. Chen, Y. Xiong, Y.-J. Xu, Dynamic evolution of atomically dispersed Cu species for CO_2 photoreduction to solar fuels, ACS Catal 9 (2019) 4824–4833.
[6] M.-Q. Yang, Y.-J. Xu, Photocatalytic conversion of CO_2 over graphene-based composites: current status and future perspective, Nanoscale Horiz. 1 (2016) 185–200.
[7] A. Galadima, O. Muraza, Catalytic thermal conversion of CO_2 into fuels : perspective and challenges, Renew. Sust. Energ. Rev. 115 (2019), 109333.
[8] J. Shi, Y. Jiang, Z. Jiang, X. Wang, X. Wang, S. Zhang, P. Han, C. Yang, Enzymatic conversion of carbon dioxide, Chem. Soc. Rev 44 (2015) 5981–6000.
[9] K.Q. Lu, Y.-H. Li, F. Zhang, M.-Y. Qi, X. Chen, Z.-R. Tang, Y.M.A. Yamada, M. Anpo, M. Conte, Y.-J. Xu, Rationally designed transition metal hydroxide nanosheet arrays on graphene for artificial CO_2 reduction, Nat. Commun. 11 (2020) 5181.
[10] M.-Y. Qi, Q. Lin, Z.-R. Tang, Y.-J. Xu, Photoredox coupling of benzyl alcohol oxidation with CO_2 reduction over CdS/TiO2 heterostructure under visible light irradiation, Appl. Catal. B: Environ. 307 (2022), 121158.
[11] Y.-H. Chen, M.-Y. Qi, Y.-H. Li, Z.-R. Tang, T. Wang, J. Gong, Y.-J. Xu, Activating two-dimensional $Ti_3C_2T_x$-MXexe with single-atom cobalt for efficient CO_2 photoreduction, Cell Reports Phys. Sci. 2 (2021), 100371.
[12] Y. Liu, B. Qu, Z. Zhang, J. Sun, X. Zhao, L. Bai, L. Jing, Synergy of dual single Ni and Co atoms on borate modified g-C_3N_4 for photocatalytic CO_2 reduction, Mater. Res. Bull. 153 (2022), 111883.
[13] C. Chen, J. Jin, S. Chen, T. Wang, J. Xiao, T. Peng, In-situ growth of ultrafine ZnO on g-C_3N_4 layer for highly active and selective CO_2 photoreduction to CH_4 under visible light, Mater. Res. Bull. 137 (2021), 111177.
[14] J.A. Oliveira, J.A. Torres, R.V. Gonçalves, C. Ribeiro, F.G.E. Nogueira, L.A. M. Ruotolo, Photocatalytic CO_2 reduction over Nb_2O_5/basic bismuth nitrate nanocomposites, Mater. Res. Bull. 133 (2021), 111073.
[15] Z. Zhu, C.-X. Yang, Y.-T. Hwang, Y.-C. Lin, R.-J. Wu, Fuel generation through photoreduction of CO_2 on novel Cu/$BiVO_4$, Mater. Res. Bull 130 (2020), 110955.
[16] H. She, Z. Zhao, W. Bai, J. Huang, L. Wang, Q. Wang, Enhanced performance of photocatalytic CO_2 reduction via synergistic effect between chitosan and Cu:TiO_2, Mater. Res. Bull. 124 (2020), 110758.
[17] G. Yin, M. Nishikawa, Y. Nosaka, N. Srinivasan, D. Atarashi, E. Sakai, M. Miyauchi, Photocatalytic carbon dioxide reduction by copper oxide nanocluster-grafted niobate nanosheets, ACS Nano 9 (2) (2015) 2111–2119.
[18] X. Zhang, Z. Yuan, J. Chen, G. Yang, D.D. Dionysiou, B. Huang, Z. Jiang, Enhanced CO_2 photoconversion activity of TiO_2 via double effect of CoPi as hole traps and high CO_2 capture, Catal. Today 340 (2020) 204–208.
[19] H. Shi, G. Chen, C. Zhang, Z. Zou, Polymeric g - C_3N_4 coupled with $NaNbO_3$ nanowires toward enhanced photocatalytic reduction of CO_2 into renewable fuel, ACS Catal. 4 (2014) 3637–3643.
[20] L. Zhang, W. Wang, H. Wang, X. Ma, Z. Bian, Molecular manganese catalyst anchored on Bi_2MoO_6 with enhanced photogenerated charges separation for efficient visible-light photoreduction of CO_2, J. Mater. Sci. Mater. Electron. 30 (2019) 5808–5819.
[21] R.C.S. Júnior, A.E. Nogueira, A.S. Giroto, J.A. Torres, C. Ribeiro, K.P.F. Siqueira, Microwave-assisted synthesis of Ca1-xMnxMoO4 (x = 0, 0.2, 0.7, and 1) and its application in artificial photosynthesis, Ceram. Int. 47 (2021) 5388–5398.
[22] Z.Q. He, L.L. Tong, Z.P. Zhang, J.M. Chen, S. Song, Ag/Ag_2WO_4 plasmonic catalyst for photocatalytic reduction of CO_2 under visible light, Acta Phys. -Chim. Sin. 31 (12) (2015) 2341–2348.
[23] H. Farsi, S. Moghiminia, M. Raygan, E. Dana, S. Hosseini, M. Behforooz, T. Zubkov, I.V. Lightcap, Z. Li, Nanostructured Tungstate-Derived Copper for Hydrogen Evolution Reaction and Electroreduction of CO_2 in Sodium Hydroxide Solutions, J. Phys. Chem. C 123 (42) (2019) 25941–25948.
[24] R. Bhosale, S. Jain, C.P. Vinod, S. Kumar, S. Ogale, Direct Z-scheme g-C_3N_4 /$FeWO_4$ nanocomposite for enhanced and selective photocatalytic CO_2 reduction under visible light, ACS Appl. Mater. Interfaces 11 (6) (2019) 6174–6183.
[25] X.Y. Kong, T. Tong, B. Ng, J. Low, T.H. Zeng, A.R. Mohamed, J. Yu, S. Chai, Topotactic transformation of bismuth oxybromide into bismuth tungstate: bandgap modulation of single-crystalline {001}-faceted nanosheets for enhanced photocatalytic CO_2 reduction, ACS Appl. Mater. Interfaces 12 (24) (2020) 26991–27000.
[26] E. Morais, K. Stanley, K.R. Thampi, J.A. Sullivan, Scope for spherical Bi_2WO_6 Quazi-Perovskites in the artificial photosynthesis reaction—the effects of surface modification with amine groups, Catal. Letters 151 (2021) 293–305.
[27] J. Mao, J. Zhao, L. Li, T. Chen, Q. Lv, Y. Li, Effect of different surfactants on the morphology, growth and magnetic behavior of $MnWO_4$ crystals via the hydrothermal method, Chinese J. Phys. 63 (2020) 163–167.
[28] M.G. Joaquín-Morales, A.F. Fuentes, S.M. Montemayor, M.J. Meléndez-Zaragoza, J.M.S. Gutiérrez, A.L. Ortiz, V. Collins-Martínez, Synthesis conditions effect on the of photocatalytic properties of $MnWO_4$ for hydrogen production by water splitting, Int. J. Hydrogen Energ. 44 (24) (2019) 12390–12398.
[29] M.H. Muhammed, B.R. Kumar, N.A. Sabu, T. Varghese, Effect of polyethylene glycol on the structural and optical properties of manganese tungstate nanorods synthesized by precipitation method, AIP Conf. Proc. 2162 (2019) 2–8.
[30] H. Cui, M. Shao, B. Li, Y. Zhang, C. Yao, Z. Li, S. Xu, Facile fabrication of $MnWO_4$/CdS composites for visible-light-driven photocatalytic Cr(VI) reduction, J. Phys. Chem. Solids 136 (2020), 109150.
[31] A.K. Chakraborty, S. Ganguli, M.A. Kebede, Photocatalytic degradation of 2-propanol and phenol using Au loaded $MnWO_4$ nanorod under visible light irradiation, J. Clust. Sci. 23 (2) (2012) 437–448.
[32] M. Tahir, B. Tahir, N.A.S. Amin, H. Alias, Selective photocatalytic reduction of CO_2 by H_2O /H_2 to CH_4 and CH_3OH over Cu-promoted In_2O_3 / TiO_2 nanocatalyst, Appl. Surf. Sci. 389 (2016) 46–55.
[33] Y.A. Sethi, A.K. Kulkarni, A.A. Ambalkar, S.K. Khore, A.R. Gunjal, S.W. Gosavi, B. B. Kale, CdS decorated $MnWO_4$ nanorod nanoheterostructures: a new 0D-1D hybrid system for enhanced photocatalytic hydrogen production under natural sunlight, Nanoscale Adv 3 (2021) 508–516.
[34] X.A. López, A.F. Fuentes, M.M. Zaragoza, J.A.D. Guillén, J.S. Gutiérrez, A.L. Ortiz, V.C. Martínez, Synthesis, characterization and photocatalytic evaluation of MWO_4

(M = Ni, Co, Cu and Mn) tungstates, Int. J. Hydrog. Energy 41 (48) (2016) 23312–23317.
[35] A. Altomare, C. Cuocci, C. Giacovazzo, A. Moliterni, R. Rizzi, QUALX: a computer program for qualitative analysis using powder diffraction data, J. Appl. Cryst. 41 (4) (2008) 815–817.
[36] M.R. Willcott, MestRe Nova, J. Am. Chem. Soc. 131 (2009) 13180.
[37] M. Rahimi-Nasrabadi, M. Eghbali-Arani, The effect of sugars on the morphology of $MnWO_4$ nanoparticles, and evaluating the product as photocatalysts, J. Mater. Sci. Mater. Electron. 28 (20) (2017) 15239–15245.
[38] M. Vosoughifar, Preparation, characterization, and morphological control of $MnWO_4$ nanoparticles through novel method and its photocatalyst application, J. Mater. Sci. Mater. Electron. 28 (2) (2017) 2135–2140.
[39] D.L. Rousseau, R.P. Bauman, S.P.S. Porto, Normal Mode Determination in Crystals and Spectroscopic Selection Rules, J. Raman Spectrosc. 10 (1) (1981) 253–290.
[40] M. Maczka, M. Ptak, K. Hermanowicz, A. Majchrowski, A. Pikul, J. Hanuza, Lattice dynamics and temperature-dependent Raman and infrared studies of multiferroic $Mn_{0.85}Co_{0.15}WO_4$ and $Mn_{0.97}Fe_{0.03}WO_4$ crystals, Phys. Rev. B - Condens. Matter 83 (17) (2011) 1–14.
[41] T. Möller, P. Becker, L. Bohatý, J. Hemberger, M. Grüninger, Infrared-active phonon modes in monoclinic multiferroic $MnWO_4$, Phys. Rev. B - Condens. Matter 90 (15) (2014) 1–16.
[42] W. Tong, L. Li, W. Hu, T. Yan, X. Guan, G. Li, Kinetic control of $MnWO_4$ nanoparticles for tailored structural properties, J. Phys. Chem. C 114 (36) (2010) 15298–15305.
[43] H.W. Wang, S.H. Zheng, G.Z. Zhou, P.Z. Chen, L. Lin, Z.B. Yan, X.H. Zhou, X. P. Jiang, H.W. Yu, J.M. Liu, The Ir^{4+} substitution dependence of electric polarization as a probe of magnetic phase stability in multiferroic $MnWO_4$, J. Appl. Phys. 126 (6) (2019), 064103.
[44] J. Ruiz-Fuertes, D. Errandonea, O. Gomis, A. Friedrich, F.J. Manjón, Room-temperature vibrational properties of multiferroic $MnWO_4$ under quasi-hydrostatic compression up to 39 GPa, J. Appl. Phys. 115 (4) (2014), 043510.
[45] K.P.F. Siqueira, A. Dias, Incipient crystallization of transition-metal tungstates under microwaves probed by Raman scattering and transmission electron microscopy, J. Nanoparticle Res. 13 (11) (2011) 5927–5933.
[46] M.V.da Silva, D.F.M.de Oliveira, H.S. Oliveira, K.P.F. Siqueira, Influence of temperature on the structural and color properties of nickel molybdates, Mater. Res. Bull. 122 (2020), 110665.
[47] R.K.S. Costa, S.C. Teles, P.C.S. Filho, A. Dias, K.P.F. Siqueira, Influence of europium doping on the structural phase-transition temperature of β− and α−$CoMoO_4$ polymorphs, Mater. Res. Bull 118 (2019), 110517.
[48] R.D. Shannon, Revised effective ionic radii and systematic studies of interatomie distances in halides and chaleogenides, Acta Cryst 32 (1976) 751–767.
[49] M. Ptak, M. MacZka, K. Hermanowicz, A. Pikul, J. Hanuza, Temperature-dependent Raman and IR studies of multiferroic $MnWO_4$ doped with Ni^{2+} ions, Spectrochim. Acta A Mol. Biomol. Spectrosc. 86 (2012) 85–92.
[50] B.L. Cushing, V.L. Kolesnichenko, C.J. O'Connor, Recent advances in the liquid-phase syntheses of inorganic nanoparticles, Chem. Rev. 104 (9) (2004) 3893–3946.
[51] M.A.P. Almeida, L.S. Cavalcante, M.S. Li, J.A. Varela, E. Longo, Structural refinement and photoluminescence properties of $MnWO_4$ nanorods obtained by microwave-hydrothermal synthesis, J. Inorg. Organomet. Polym. Mater. 22 (1) (2012) 264–271.
[52] P.V. Hanh, L.H. Hoang, P.V. Hai, N.V. Minh, X.B. Chen, I.S. Yang, Crystal quality and optical property of $MnWO_4$ nanoparticles synthesized by microwave-assisted method, J. Phys. Chem. Solids 74 (3) (2013) 426–430.
[53] M. Hämmer, O. Janka, J. Bönnighausen, S. Klenner, R. Pöttgen, H.A. Höppe, On the phosphors $Na_5M(WO_4)_4$ (M = Y, La-Nd, Sm-Lu, Bi)-crystal structures, thermal decomposition, and optical and magnetic propertie, Dalton. Trans 49 (24) (2020) 8209–8225.
[54] D.L. Wood, Weak absorption tails in amorphous semiconductors, Phys. Rev. B 5 (8) (1972) 3144–3151.
[55] A.E. Morales, E.S. Mora, U. Pal, Use of diffuse reflectance spectroscopy for optical characterization of un-supported nanostructures, Rev. Mex. Física 53 (5) (2007) 18–22.
[56] P. Mal, P. Rambabu, G.R. Turpu, A.K. Gupta, B. Chakraborty, P. Sem, P. Das, Energy band gap and spectroscopic studies in $Mn_{1-x}Cu_xWO_4$ ($0 \leq x \leq 0.125$), AIP Conf. Proc 1728 (2016) 1–5.
[57] W. Zhang, Y. Hu, L. Ma, G. Zhu, Y. Wang, X. Xue, R. Chen, S. Yang, Z. Jin, Progress and perspective of electrocatalytic CO_2 reduction for renewable carbonaceous fuels and chemicals, Adv. Sci. 5 (1) (2018), 1700275.
[58] K.P. Kuhl, E.R. Cave, D.N. Abram, T.F. Jaramillo, New insights into the electrochemical reduction of carbon dioxide on metallic copper surfaces, Energy Environ. Sci. 5 (2012) 7050–7059.
[59] X. Zhao, L. Du, Y.Sun B.You, Integrated design for electrocatalytic carbon dioxide reduction, Catal. Sci. Technol 10 (2020) 2711–2720.
[60] L.S. Ribeiro, I.M. Pinatti, J.A. Torres, A.S. Giroto, F. Lesse, E. Longo, C. Ribeiro, A. E. Nogueira, Rapid microwave-assisted hydrothermal synthesis of $CuBi_2O_4$ and its application for the artificial photosynthesis, Mater. Lett. 275 (2020), 128165.
[61] A.E. Nogueira, G.T.S.T. Silva, J.A. Oliveira, O.F. Lopes, J.A. Torres, M. Carmo, C. Ribeiro, CuO decoration controls Nb_2O_5 photocatalyst selectivity in CO_2 reduction, ACS Appl. Energy Mater. 3 (8) (2020) 7629–7636.
[62] A. Malekzadeh, M. Abedini, A.A. Khodadadi, M. Amini, H.K. Mishra, A.K. Dalai, Critical influence of Mn on low-temperature catalytic activity of $Mn/Na_2WO_4/SiO_2$ catalyst for oxidative coupling of methane, Catal. Lett. 84 (1) (2002) 45–51.
[63] A. Malekzadeh, A. Khodadadi, A.K. Dalai, M. Abedini, Oxidative coupling of methane over lithium doped (Mn+ W)/SiO_2 catalysts, J. Nat. Gas Chem. 16 (2) (2007) 121–129.
[64] N.Y. Dzade, CO_2 and H_2O coadsorption and reaction on the low-index surfaces of tantalum nitride: a first-principles DFT-D3 investigation, Catalysts 10 (2020) 1217.
[65] Y. Song, W. Chen, W. Wei, Y. Sun, Advances in clean fuel ethanol production from electro-, photo- and photoelectro- catalytic CO_2 reduction, Catalysts 10 (2020) 1287.